CHEX-MATE: Turbulence in the intra-cluster medium from X-ray surface brightness fluctuations

S. Dupourqué, N. Clerc, E. Pointecouteau, D. Eckert, M. Gaspari, L. Lovisari, G. W. Pratt, E. Rasia, M. Rossetti, F. Vazza, et al.

A&A, 687, A58 (2024)
https://doi.org/10.1051/0004-6361/202348701

Astronomy & Astrophysics

CHEX-MATE: Turbulence in the intra-cluster medium from X-ray surface brightness fluctuations

S. Dupourqué[1], N. Clerc[1], E. Pointecouteau[1], D. Eckert[2], M. Gaspari[3], L. Lovisari[4,5], G. W. Pratt[6], E. Rasia[7,8], M. Rossetti[9], F. Vazza[10,11,12], M. Balboni[9,13], I. Bartalucci[9], H. Bourdin[15,16], F. De Luca[15,16], M. De Petris[14], S. Ettori[12], S. Ghizzardi[9], and P. Mazzotta[15,16]

[1] IRAP, Université de Toulouse, CNRS, CNES, UT3-PS, Toulouse, France
e-mail: sdupourque@irap.omp.eu
[2] Department of Astronomy, University of Geneva, Ch. d'Ecogia 16, 1290 Versoix, Switzerland
[3] Department of Astrophysical Sciences, Princeton University, 4 Ivy Lane, Princeton, NJ 08544-1001, USA
[4] Dipartimento di Fisica e Astronomia, Universitá di Bologna, Via Gobetti 93/2, 40122 Bologna, Italy
[5] Center for Astrophysics | Harvard & Smithsonian, 60 Garden Street, Cambridge, MA 02138, USA
[6] Université Paris-Saclay, Université Paris Cité, CEA, CNRS, AIM, 91191 Gif-sur-Yvette, France
[7] INAF, Osservatorio di Trieste, v. Tiepolo 11, 34131 Trieste, Italy
[8] IFPU, Institute for Fundamental Physics of the Universe, Via Beirut 2, 34014 Trieste, Italy
[9] Istituto Nazionale di Astrofisica, IASF-Milano, Via A. Corti 12, 20133 Milano, Italy
[10] Hamburger Sternwarte, University of Hamburg, Gojenbergsweg 112, 21029 Hamburg, Germany
[11] Istituto di Radioastronomia, INAF, Via Gobetti 101, 40122 Bologna, Italy
[12] INAF, Osservatorio di Astrofisica e Scienza dello Spazio, Via Piero Gobetti 93/3, 40129 Bologna, Italy
[13] DiSAT, Università degli Studi dell'Insubria, Via Valleggio 11, 22100 Como, Italy
[14] Dipartimento di Fisica, Sapienza Università di Roma, Piazzale Aldo Moro 5, 00185 Roma, Italy
[15] Università degli studi di Roma "Tor Vergata", Via della ricerca scientifica, 1, 00133 Roma, Italy
[16] INFN, Sezione di Roma 2, Università degli studi di Roma Tor Vergata, Via della Ricerca Scientifica, 1, Roma, Italy

Received 22 November 2023 / Accepted 4 March 2024

ABSTRACT

The intra-cluster medium is prone to turbulent motion that will contribute to the non-thermal heating of the gas, complicating the use of galaxy clusters as cosmological probes. Indirect approaches can estimate the intensity and structure of turbulent motions by studying the associated fluctuations in gas density and X-ray surface brightness. In this work, we aim to constrain the gas density fluctuations occurring in the CHEX-MATE sample to obtain a detailed view of their properties in a large population of clusters. To do so, we use a simulation-based approach to constrain the parameters of the power spectrum of density fluctuations, assuming a Kolmogorov-like spectrum and including the stochastic nature of the fluctuation-related observables in the error budget. Using a machine-learning approach, we learn an approximate likelihood for each cluster. This method requires clusters not to be too disturbed, as fluctuations can originate from dynamic processes such as merging. Accordingly, we removed the less relaxed clusters (centroid shift $w > 0.02$) from our sample, resulting in a sample of 64 clusters. We defined different subsets of CHEX-MATE to determine properties of density fluctuations as a function of dynamical state, mass, and redshift, and we investigated the correlation with the presence or not of a radio halo. We found a positive correlation between the dynamical state and density fluctuation variance, a non-trivial behaviour with mass, and no specific trend with redshift or the presence of a radio halo. The injection scale is mostly constrained by the core region. The slope in the inertial range is consistent with the Kolmogorov theory. When interpreted as originating from turbulent motion, the density fluctuations in R_{500} yield an average Mach number of $\mathcal{M}_{3D} \simeq 0.4 \pm 0.2$, an associated non-thermal pressure support of $P_{turb}/P_{tot} \simeq (9 \pm 6)\%$, or a hydrostatic mass bias $b_{turb} \simeq 0.09 \pm 0.06$. These findings align with expectations from existing literature.

Key words. turbulence – galaxies: clusters: intracluster medium – X-rays: galaxies: clusters

1. Introduction

Clusters of galaxies, which are the largest gravitationally bound structures in the Universe, house the majority of their baryonic content within the intra-cluster medium (ICM). This hot gas ($\sim 10^7 - 10^8$ K) quickly develops turbulent cascades as a result of the various perturbations it undergoes. Different phenomena will dictate the injection of kinetic energy into the ICM, depending on the location within the cluster. The central parts are dominated by feedback from the active galactic nucleus (AGN; McNamara & Nulsen 2012; Gaspari et al. 2014a; Voit et al. 2017), while the outer parts are prone to accretion from the cosmic web and merging with groups or clusters of galaxies that induce shocks and therefore turbulence (Nelson et al. 2012). These perturbations and their associated turbulence significantly contribute to the non-gravitational heating of the ICM, thereby influencing the hydrostatic mass bias of galaxy clusters (Piffaretti & Valdarnini 2008; Lau et al. 2009; Rasia et al. 2012; Nelson et al. 2014; Biffi et al. 2016; Pratt et al. 2019; Gianfagna et al. 2023).

Generally speaking, turbulence is characterised by chaotic, irregular motion in a fluid resulting from the injection of high-scale kinetic energy and high Reynolds numbers. It involves the transfer of energy from large scales to smaller scales

within the fluid, leading to complex, unpredictable patterns of motion. Turbulence in galaxy clusters is extensively modelled through numerical simulations (e.g. Vazza et al. 2012; Schmidt et al. 2016; ZuHone et al. 2018; Mohapatra & Sharma 2019; Ayromlou et al. 2023). Studying turbulence in galaxy clusters can help in characterising the non-thermal pressure support of the ICM, as this should be one of its key components (Vazza et al. 2018; Angelinelli et al. 2020), together with magnetic fields and, to a lesser extent, cosmic rays.

Constraining this process is relatively straightforward with highly resolved X-ray information in the spectral domain, as the motion of the gas is mirrored in the observed spectrum through centroid shifts and the broadening of the emission lines. Direct measurements of the line centroid shift were performed with the XIS instrument onboard *Suzaku*, deriving upper limits as a subsonic line-of-sight motion in local clusters of various dynamical states (Ota et al. 2007; Sugawara et al. 2009; Tamura et al. 2011, 2014; Ota & Yoshida 2016). More recently, by calibrating the EPIC-pn instrument of *XMM-Newton* using the instrumental fluorescence lines, measurements of velocity maps with a precision level of $\sim$200−500 km s^{-1} were performed for local clusters, and the first centroid shift structure function from direct observations was derived (Gatuzz et al. 2022a,b, 2023a,b). Broadening measurements were performed using the RGS instrument of *XMM-Newton* (Sanders et al. 2011; Sanders & Fabian 2013; Pinto et al. 2015; Ogorzalek et al. 2017), providing overall upper limits on subsonic motions. A comprehensive review of the study of the ICM motion is proposed by Simionescu et al. (2019). Calibration uncertainties and limited spatial resolution are the main showstoppers when studying the ICM motions in the X-ray domain. The emergence of X-ray integral field units will enable high-precision direct measurements of such turbulent motions (e.g. Roncarelli et al. 2018; Zhang et al. 2024). The Hitomi Collaboration (2016) determined a line-of-sight velocity dispersion of $\sim$160 km s^{-1} in the core of Perseus cluster. Similar measurements will be accessible with the recent launch of XRISM/Resolve (XRISM Science Team 2020), the Line Emission Mapper (LEM, Kraft et al. 2022), and *Athena*/X-IFU in the long term (Barret et al. 2020). Indirect measurements can be achieved by searching for fluctuations in the thermodynamical properties of the ICM that can be due to turbulent processes. For instance, X-ray surface brightness (X-SB) fluctuations point to a pure hydrodynamical flow in the ICM (Schuecker et al. 2004). Such methods have been applied to the Coma (Churazov et al. 2012; Gaspari & Churazov 2013) and Perseus cluster (Zhuravleva et al. 2015). Zhuravleva et al. (2018) used a small sample of clusters to investigate the turbulent motions occuring in their cool-cores. Hofmann et al. (2016) investigated the fluctuations of several thermodynamical properties of the ICM. Khatri & Gaspari (2016) and Romero et al. (2023) showed a promising approach, joining the X-ray images to the Sunyaev-Zel'dovich effect (SZE).

These studies do not account for the stochastic nature of the surface brightness fluctuations. Indeed, when observing a random field with a finite size sample and trying to assess its properties, an additional source of irreducible variance is added to the total error budget. As shown in Clerc et al. (2019) and in Cucchetti et al. (2019), the so-called sample variance may be dominant at any spatial scale achievable by *XMM-Newton*, and its prevalence grows with scale up to an order of magnitude with respect to other sources. In Dupourqué et al. (2023), we performed an X-ray surface brightness fluctuation analysis on the X-COP cluster sample (Eckert et al. 2017a), with a forward model approach to explicitly account for the sample variance. In this work, we applied this approach to the CHEX-MATE cluster sample, which is an order of magnitude higher in terms of statistics and contains a more diverse population of clusters.

In Sect. 2, we describe the methodology to compute the density fluctuation parameters. In Sect. 3, we present the joint constraints on density fluctuations -applied to various sub-samples of CHEX-MATE- show the effect of excluding the central part of clusters in our analysis, and investigate the correlation with radio data using the LOw Frequency ARray (LOFAR) Two Meter Sky Survey second data release (LoTSS DR2, Shimwell et al. 2022; Botteon et al. 2022). In Sect. 4, we discuss the Mach number obtained when assuming that the density fluctuations originate from turbulent processes, and the resulting turbulent mass bias. Throughout this paper, we assume a flat ΛCDM cosmology with $H_0 = 70\,\mathrm{km\,s^{-1}}$ and $\Omega_m = 1 - \Omega_\Lambda = 0.3$. Scale radii are defined according to the critical density of the Universe at the corresponding redshift. The R_{500} and M_{500} values are obtained from the MMF3 detection method (Melin et al. 2006) as highlighted in Appendix A of CHEX-MATE Collaboration (2021). The Fourier transform conventions are highlighted in Appendix A.

2. Data and method

2.1. The CHEX-MATE sample

The CHEX-MATE programme[1], detailed in CHEX-MATE Collaboration (2021), is a three mega-second, multi-year *XMM-Newton* Heritage programme aimed at obtaining X-ray observations of 118 minimally biased, signal-to-noise-limited galaxy clusters detected by Planck through SZE (Planck Collaboration XXVII 2016). The project's objectives are to accurately understand the statistical properties of the cluster population, examine how gas properties are influenced by dark-matter halo collapse, reveal non-gravitational heating origins, and address major uncertainties in mass determination that restrict the use of clusters for cosmological parameter estimation.

To achieve these goals, a sample of 118 Planck clusters was chosen based on their SZE signal ($S/N > 6.5$) and categorised into two sub-samples: Tier 1 contains 61 low-redshift objects in the northern sky that provide an unbiased view of the most recent cluster population ($0.05 < z < 0.2$ and $2 < \frac{M_{500}}{10^{14}\,M_\odot} < 9$); Tier 2 is representative of the most massive systems formed in the Universe's history ($z < 0.6$ and $\frac{M_{500}}{10^{14}\,M_\odot} > 7.25$). These sub-samples share four common clusters. The *XMM-Newton* observations are characterised by an exposure time ensuring an S/N of 150 within R_{500} in the [0.3–2.0] keV band. This requirement was chosen to satisfy three conditions: (i) to calculate the temperature profile up to R_{500} (with an accuracy level of ±15% in the [0.8–1.2] R_{500} region); (ii) to measure the mass obtained from the Y_X mass proxy (Kravtsov et al. 2006), in which $Y_X = M_{g,500}T_X$ ($M_{g,500}$ represents the gas mass within R_{500} and T_X refers to the spectroscopic temperature estimated in the [0.15–0.75] R_{500} range), with an uncertainty of ±2%; and (iii) to derive the mass derived from hydrostatic equilibrium (HE) at R_{500} with a precision level of approximately 15−20%. For further information on the sample, scientific objectives, and observation strategies in X-ray and other wavebands, readers should consult the presentation paper: CHEX-MATE Collaboration (2021).

[1] http://xmm-heritage.oas.inaf.it/

2.2. Data preparation

The images in this study were generated using the pipeline established for the X-COP sample (Eckert et al. 2017a; Ghirardini et al. 2019) and adopted by the CHEX-MATE collaboration. Specifically, *XMM-Newton* data were processed with SAS software (version 16.1.0) and the Extended Source Analysis Software package (ESAS, Snowden et al. 2008). The choice of SAS version 16.1 is motivated in Rossetti et al. (2024), to which we refer the reader for more details. In brief, we aim to avoid the presence of unresolved bugs in intermediate versions of SAS and a major refactoring effort for version 21.0, which makes existing reduction pipelines incompatible for the time being. However, we ensured that the latest calibration from January 2021 was applied, as specified by Bartalucci et al. (2023). Count images, exposure maps, and particle background maps were extracted in the narrow [0.7–1.2] keV band to maximise the source-to-background emission ratio and minimize systematics related to EPIC background subtraction. A detailed account of the procedure is presented in Bartalucci et al. (2023), and a complete gallery of images is displayed in Fig. 6 in CHEX-MATE Collaboration (2021). Point sources are extracted using the `ewavelet` routine in the two energy bands [0.3–2] and [2–7] keV. Every source with flux smaller than the maximum of the log N–log S distribution determined from the point source extraction is masked.

2.3. Bayesian inference for density fluctuations

The methodology described below was first developed and discussed in detail in Dupourqué et al. (2023). This is a three-step procedure that consists of determining an unperturbed surface brightness model, defining the associated surface brightness fluctuations and deriving a meaningful observable, and finally constraining parameters of the 3D power spectrum, including the whole error budget. We summarise it briefly in the following sections, but refer we interested readers to the aforementioned publication for further details.

2.3.1. X-SB unperturbed model

In this study, we aim to model the unperturbed surface brightness S_X of a galaxy cluster to define fluctuations. Using $\boldsymbol{r} = (x, y, \ell)$ as the 3D position parametrisation and $\boldsymbol{\rho} = (x, y)$ as the 2D equivalent, the surface brightness can be expressed as

$$S_X(\boldsymbol{\rho}) = \int_{-\infty}^{+\infty} \Psi(\boldsymbol{r})\, n_e^2(\boldsymbol{r})\, \mathrm{d}\ell + B,$$

where $n_e(\boldsymbol{r})$ is the electronic density and $\Psi(\boldsymbol{r})$ represents a combination of various factors such as the cooling function, cosmological dimming, Galactic absorption, and convolution with the XMM response functions. B denotes a constant surface brightness sky background. This radial model is folded in a triaxial shape for the cluster, with no scaling along the line of sight. The centre position and ellipticity are left free, and the centre is fitted with a normal prior centred on the X-ray peak as defined by Bartalucci et al. (2023), with a 50% relative scatter. A modified Vikhlinin model (with $\alpha = 0$ and $\gamma = 3$, see Vikhlinin et al. 2006; Shi et al. 2016) is used to parametrise the density profile:

$$n_e(r) = n_{e,0} \frac{(1 + r^2/r_c^2)^{-3\beta/2}}{(1 + r^3/r_s^3)^{\epsilon/6}}.$$

The $\Psi(\boldsymbol{r})$ function is determined using an analytical functional form that we fit on a count-rate grid estimated using `XSPEC 12.11.1`. To do so, we compute the expected count-rate of a `PhAbs*APEC` model with the same instrumental setup and redshift for each cluster in the CHEX-MATE sample; more details are available in Appendix C of Dupourqué et al. (2023). The metallicity was set to $0.3\,Z_\odot$ and the abundances fixed according to Anders & Grevesse (1989). Galactic absorption is accounted for using the N_H data from the HI4PI survey (HI4PI Collaboration 2016). The count image is rebinned using Voronoi tessellation (Cappellari & Copin 2003), with approximately 100 counts per bin, to increase the speed of the inference given the computationally intense surface brightness model that we consider. This binning introduces a median bias of ∼0.5%, which peaks at 4% in the outermost (and low-significance) region, which is still lower than the expected 10% systematic error due to Poisson noise (see Appendix D in Dupourqué et al. 2023 for more details). The number of counts expected in each bin is forward modelled using the aforementioned surface brightness model. The model parameters are determined using Bayesian inference with a Poisson likelihood in each bin. The posterior distributions are sampled using the No U-Turn Sampler (Hoffman & Gelman 2014) as implemented in the `numpyro` library (Bingham et al. 2019; Phan et al. 2019).

2.3.2. Surface brightness and density fluctuations

Surface brightness emission from galaxy clusters in the soft X-ray band originates mainly from the thermal bremsstrahlung occurring in the ICM plasma. The intensity of this radiation is directly proportional to the squared electronic density. Hence, over-densities and under-densities in the gas distribution can be found as fluctuations in the surface brightness images, and they dominate the fluctuations when compared to other sources (Churazov et al. 2012). To constrain the properties of the density fluctuations, we chose to model it as a Gaussian random field, which can be described using only a second-order moment such as the power spectrum or the structure function. As we expect a strong link between density fluctuations and turbulence (Gaspari & Churazov 2013; Gaspari et al. 2014b; Zhuravleva et al. 2014a; Simonte et al. 2022), we model the 3D power spectrum of the random field using a Kolmogorov-like functional form (e.g. ZuHone et al. 2016; Dupourqué et al. 2023) since turbulence in clusters is compatible with the purely hydrodynamical case (Schuecker et al. 2004):

$$\mathcal{P}_{3\mathrm{D},\delta}(k) = \sigma_\delta^2 \frac{e^{-\left(k/k_{\mathrm{inj}}\right)^2} e^{-(k_{\mathrm{dis}}/k)^2} k^{-\alpha}}{\int 4\pi k^2\, e^{-\left(k/k_{\mathrm{inj}}\right)^2} e^{-(k_{\mathrm{dis}}/k)^2} k^{-\alpha} \mathrm{d}k}, \quad (1)$$

where k_{inj} and k_{dis} are, respectively, the Fourier frequencies corresponding to the injection scale ℓ_{inj} and dissipation scale ℓ_{dis}, α is the inertial range spectral index (shortened to "slope"), and σ_δ^2 is the variance of fluctuations. We fix the dissipation scale for our entire sample at $10^{-3}\,R_{500}$ (e.g. Brüggen & Vazza 2015), which is significantly smaller than the spatial scales accessible with CHEX-MATE ($\gtrsim 10^{-2}\,R_{500}$. In any case, the arbitrary choice of dissipation scale has little to no impact on the normalisation of the power spectrum.

2.3.3. X-SB fluctuations and power spectrum

In this analysis, the X-SB fluctuations are assumed to originate exclusively from intrinsic density fluctuations (see Churazov et al. 2012 for other sources of X-SB fluctuations). The squared density profile can be split into a rest component

$n^2_{e,0}$ and fluctuations $\delta \ll 1$, such that the density is given by $n_e(\boldsymbol{r}) = n_{e,0}(\boldsymbol{r}) \times (1 + \delta(\boldsymbol{r}))$. Using a first-order expansion of the density, the raw surface brightness image $S_X(\boldsymbol{\rho})$ can be decomposed as the sum of an unperturbed image $S_{X,0}(\boldsymbol{\rho})$ and a surface brightness fluctuation map. We define the fluctuation map as follows:

$$\Delta(\boldsymbol{\rho}) \overset{\text{def}}{=} \frac{S_X(\boldsymbol{\rho}) - S_{X,0}(\boldsymbol{\rho})}{2} \simeq \int_{-\infty}^{+\infty} \epsilon_0(\boldsymbol{r})\delta(\boldsymbol{r})\mathrm{d}\ell, \tag{2}$$

where $S_{X,0}$ can be obtained using the best-fit X-SB model and $\epsilon_0(\boldsymbol{r}) = \Psi(\boldsymbol{r})\ n^2_{e,0}(\boldsymbol{r})$ is the associated best-fit emissivity. The factor two arises when considering the square dependency of δ with the surface brightness. To study the contribution of each spatial scale to surface brightness fluctuations, an analysis in Fourier space is performed. We note the Fourier 3D frequencies such as $\boldsymbol{k} = (k_x, k_y, k_\ell)$, and associated 2D frequencies such as $\boldsymbol{\kappa} = (k_x, k_y) = (\kappa, \varphi_k)$ in cylindrical coordinates. The power spectrum of the fluctuations, $\mathcal{P}_{\mathrm{2D},\Delta}$, is defined as

$$\mathcal{P}_{\mathrm{2D},\Delta}(\kappa) = \frac{1}{2\pi} \int |\hat{\Delta}(\boldsymbol{\kappa})|^2 \mathrm{d}\varphi_k,$$

where $\hat{\Delta}$ is the Fourier transform of the 2D map Δ and φ is the direction angle in Fourier space. The numerical evaluation of $P_{\mathrm{2D},\Delta}$ is performed using the method described by Arévalo et al. (2012), which computes the variance of images filtered by Mexican hats on a characteristic scale to estimate the power spectrum, implicitly handling irregular masks such as the excluded point sources or *XMM-Newton* mosaics. In practice, we divide the X-SB fluctuation power spectrum $\mathcal{P}_{\mathrm{2D},\Delta}$ by the power spectrum of the best-fit X-SB model with Poisson noise $\mathcal{N}_{\mathrm{2D},\Delta}$, to isolate exclusively the fluctuations due to density variations. This observable is defined as a signal-to-noise ratio (S/N) as follows:

$$S/N_\Delta \overset{\text{def}}{=} \frac{\mathcal{P}_{\mathrm{2D},\Delta}}{\mathcal{N}_{\mathrm{2D},\Delta}}. \tag{3}$$

We compute this spectrum on scales defined by the size of the cluster in R_{500} units. The observational strategy detailed in CHEX-MATE Collaboration (2021) and Rossetti et al. (2024) ensures that the thermodynamic properties can be reconstructed up to R_{500}, so we use photons inside this radius. Since the CHEX-MATE sample has a wide range of redshifts, the lowest scale we can investigate is greater for distant clusters than for nearby clusters. We choose a conservative, redshift-dependent scale that allows us to study all clusters respecting the Nyquist–Shannon criterion and minimising the lost information, in the form of an affine function:

$$\rho_{\mathrm{low}} \simeq 0.123 \times z + 0.023\ \ [R_{500}]\,. \tag{4}$$

The lowest scale for each cluster in the sample as a function of z is displayed in Fig. 1, where Eq. (4) is shown with a dotted line. The effect of this redshift-dependent scale will be to reduce the importance of distant clusters compared with closer ones, since the information linked to them is intrinsically less constraining.

2.3.4. Simulation-based inference

To link our observable quantities to the parameters of the density fluctuations, we need to establish the formal link between these two quantities, which is encapsulated by the likelihood function in a Bayesian framework. However, we cannot derive an analytical formula or closed form for this likelihood in this case. It is, however, possible to generate mock observables by generating a Gaussian random field with known parameters and injecting it into our best-fit emissivity model before projection along the line of sight. By including all our sources of uncertainty in this forward modelling, it is possible to assess the dispersion associated with our parameters and our observable due to the sample variance and Poisson noise. This procedure is repeated for 300 000 simulations per cluster to build the training sample, whose generating parameters are randomly drawn from the following priors: $\sigma_\delta \sim 10^{\mathcal{U}(-2,0)}$, $\ell_{\mathrm{inj}} \sim 10^{\mathcal{U}(-2,0.3)}$, and $\alpha \sim \mathcal{U}(2,5)$. We showed in Dupourqué et al. (2023) that this amount of simulations is sufficient to build a likelihood estimator enabling the reconstruction of the expected parameters for mock observations. We train a neural network on these simulations to estimate an approximation of the likelihood of our problem, using a masked autoregressive flow (Papamakarios et al. 2017, 2019) as implemented in the `sbi` package (Tejero-Cantero et al. 2020). In a nutshell, a masked autoregressive flow is a density estimator that is adjusted to estimate any well-behaved distribution (in the mathematical sense). In this problem, the likelihood of a specific observation is learned from the 300 000 joint samples of parameters and mock observations. Once it is trained, the model can return an approximation of the likelihood of any observation. This approximate likelihood is sampled and inverted into a posterior distribution using classical MCMC methods such as NUTS (Hoffman & Gelman 2014).

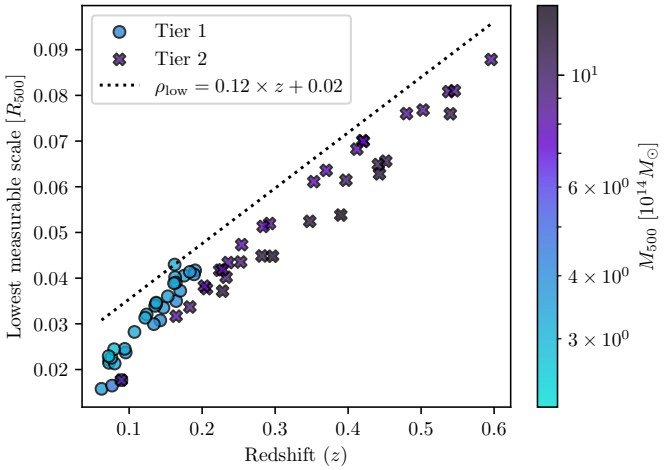

Fig. 1. Lowest scale accessible as a function of the redshift and best conservative affine relationship used in this work as defined in Eq. (4), which is defined as an affine function with the same slope as the points, but increased above them.

2.4. Splitting CHEX-MATE into sub-samples

The presented methodology allows the estimation of the likelihood of individual observations of each cluster. By joining them, one can estimate the parameters of the density fluctuations on selected subsets of the CHEX-MATE sample. For this study, we exclude some clusters for quality or modelling reasons. Our modelling is effective on regular clusters. Disturbed clusters, which have strong departures from spherical symmetry, produce very inhomogeneous density fluctuations due to structural residues. It is important to emphasize that the descriptive power of the Gaussian field model decreases in clusters featuring structures resulting from its dynamic assembly, such as sloshing spirals or cool cores. To mitigate this effect, we want to

Table 1. Definition of the sub-samples used in the analysis and relative size of each sample.

Sub-sample	Definition	Size
State (I)	$0.001 < w < 0.005$	22
State (II)	$0.005 < w < 0.011$	21
State (III)	$0.011 < w < 0.019$	21
Mass (I)	$2.2 < M_{500} < 3.77$	11
Mass (II)	$3.77 < M_{500} < 4.65$	10
Mass (III)	$4.65 < M_{500} < 8.77$	10
Redshift (I)	$0.09 < z < 0.26$	12
Redshift (II)	$0.26 < z < 0.42$	11
Redshift (III)	$0.42 < z < 0.6$	11
Radio halo	Halo in LoTSS DR2	8
No radio halo	No halo in LoTSS DR2	13

Notes. The total number of clusters used in the analysis is 64. Masses are in $10^{14}\ M_\odot$ units.

systematically exclude clusters to which this approach is not suited and use morphological indicators to do so. Campitiello et al. (2022) extracted morphological parameters of the CHEX-MATE sample and compared it to a visual classification in three classes: (i) relaxed, (ii) mixed, (iii) disturbed. The centroid shift w, which relates to the variation of the distance of the peak of luminosity and the centroid of the emission for a varying aperture up to R_{500}, was computed for every cluster in the CHEX-MATE sample, and it shows good separation of the three states. This quantity is dimensionless as it is scaled to R_{500}. We chose to exclude clusters such as $w > 0.02$, which is comparable to the threshold proposed by Lovisari et al. (2017) to classify disturbed clusters and corresponds to 43 objects in the whole CHEX-MATE sample. Campitiello et al. (2022) also derived a combined M parameter (see also Rasia et al. 2013; De Luca et al. 2021), the purpose of which was to estimate the disturbance of clusters on a continuum using a combination of multiple morphological indicators. Using w or M yields similar results in this study, as both can define a threshold to exclude the most visually disturbed clusters. However, using w instead of M removes more mixed clusters from the sample with the same threshold definition, which is arguably a more conservative choice. Finally, w correlates better with the variance of density fluctuations than M in the whole sample, with a Pearson R of 0.5 and 0.36, respectively, showing that w is, in this case, more suitable to track the surface brightness disturbances. It is worth noting that despite this threshold, some disturbed clusters remain in our sample, such as PSZ2G266.04−21.25, which is the famous Bullet Cluster, using either criteria to perform the selection. Along with this disturbance threshold, we have systematically excluded double clusters and clusters that are contaminated by the Galactic emission (in particular CIZA clusters; see Ebeling et al. 2000), Virgo emission, or by clusters in the foreground or background.

Applying this selection leads to a set of 64 clusters, which is ∼60% of the total cluster number in CHEX-MATE. This set is divided into several sub-samples, which are defined in Table 1. For each sub-sample, the symbols (I), (II), and (III) denote an increase in the quantity used to define it; for instance, State (I) contains the most relaxed clusters, while State (III) contains the most disturbed ones. In particular, we are interested in the dependence of the density fluctuation parameters on the mass of the clusters, their redshift, and their dynamical state. The sample is divided into bins of almost equal sizes to have comparable statistics. The CHEX-MATE sample is built on two subsamples, Tier 1 and Tier 2, which are respectively made up of close clusters of varying mass, and high-mass clusters of varying redshifts. Hence, we perform mass separation using Tier 1 and redshift separation using Tier 2. The dynamical state separation is performed on the whole sample based on the parameter w. The CHEX-MATE sample is also partially observed by LOFAR. We use the radio halo data and power from the LoTSS-DR2 (Botteon et al. 2022). This survey covers 40 clusters from the CHEX-MATE sample, in which 18 admit detected radio haloes. We apply the same filtering procedure and exclude the most disturbed clusters as done previously, lowering the number of clusters to eight with a halo and 13 without a halo. To investigate the correlation between X-SB fluctuations and radio data, we further define two sub-samples of clusters containing (or not) a radio halo. The good mixing between mass, redshift, dynamical state, and the presence of a radio halo is shown in Fig. 2, guaranteeing that we are not introducing any selection bias with our sub-sample definition.

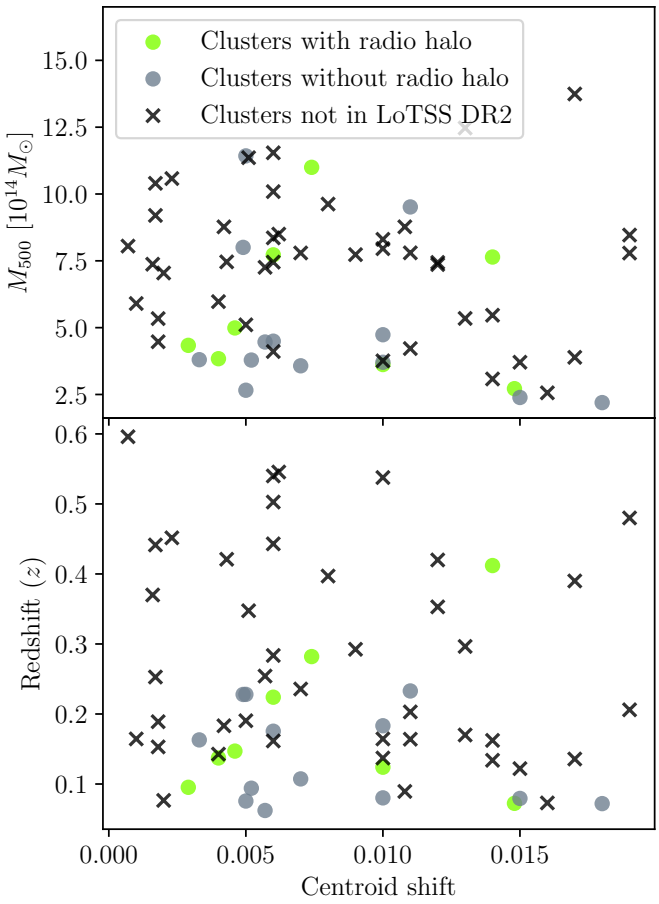

Fig. 2. Correlation between mass M_{500}, redshift z, and centroid shift w in CHEX-MATE sample without disturbed or contaminated clusters, including the clusters in LoTSS DR2 with and without radio haloes.

3. Results

3.1. Joint constraints on the sample

The constraints on surface brightness fluctuations can be significantly affected by sample variance when each cluster is studied individually. To mitigate this effect and increase the overall signal, we combine the analysis of density fluctuation properties

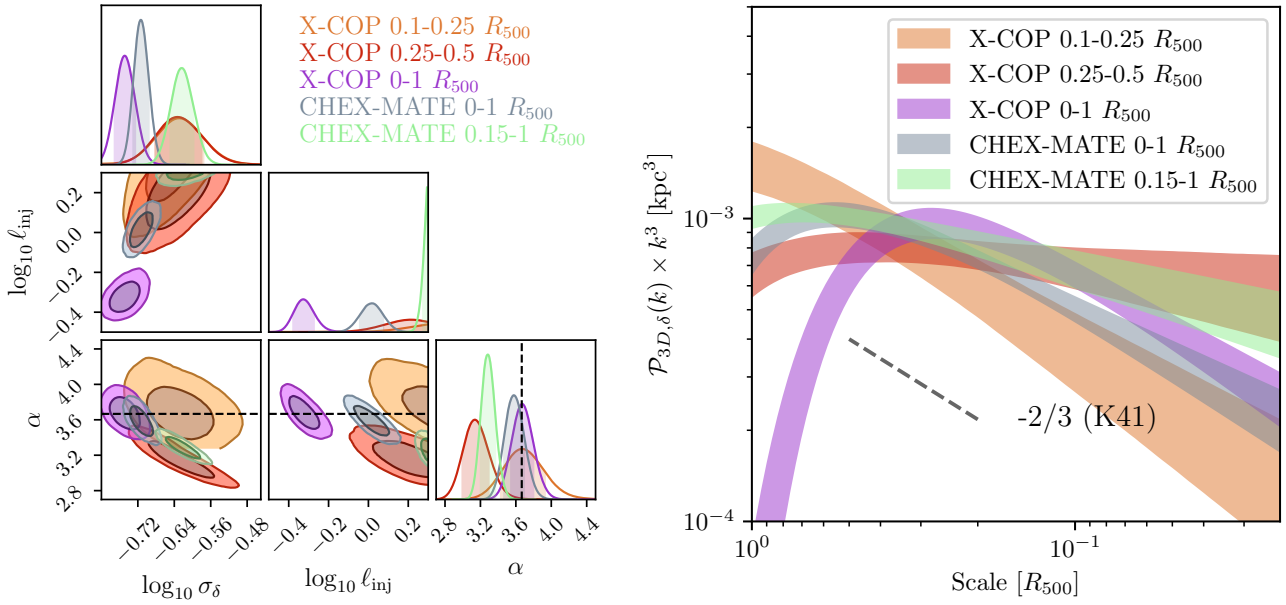

Fig. 3. Density fluctuation parameters and associated 3D power spectra for the CHEX-MATE and X-COP cluster samples for various regions of interest. Left: Joint posterior distributions of standard deviation, σ_δ, injection scale, $\ell_{\rm inj}$, and spectral index, α, of density fluctuation power spectrum parameters, estimated on the cleaned CHEX-MATE sample and with the X-COP parameters in the 0.1–0.25 and 0.25–0.5 R_{500} rings, as computed in Dupourqué et al. (2023). The dashed black line represents the expected 11/3 index from Kolmogorov theory. Right: Associated 3D power spectra as defined from Eq. (1). The dashed slope indicates the expected slope from Kolmogorov. The scales are in units of R_{500}.

across multiple clusters by summing their log-likelihoods. We calculate the X-SB fluctuation spectra using information within the R_{500} radius. As cluster cores are often contaminated by cool-cores and structural residuals, we investigate the impact of excluding the central part up to 0.15 R_{500} from our analysis. The joint parameters of the density fluctuations and their associated power spectra, estimated across the CHEX-MATE sample without disturbed clusters (64 objects), are shown in Fig. 3 and in Tables B.1 and B.2, both with and without core exclusion. These are compared with the previous results on the X-COP sample, including the constraints from Dupourqué et al. (2023) for the two rings between 0.1–0.25 and 0.25–0.5 R_{500}, as well as the entire R_{500} area. The results obtained for the fluctuation variance σ_δ and the slope α of CHEX-MATE are structurally compatible with the X-COP 0.1–0.25 and 0.25–0.5 R_{500} rings, except for the injection scale $\ell_{\rm inj}$. This is further discussed in Sect. 3.2. The slope of the CHEX-MATE analysis including the core, as in X-COP, is fully compatible with the K41 theory of Kolmogorov (1941).

The posterior distributions obtained for the joint fit across the state, mass, and redshift sub-samples, as defined in Table 1, are illustrated in Fig. 4b when the core is included and in Fig. 4c where the core is excluded. The separation of the dynamical states (Figs. 4d and g) shows an increase in the variance of the fluctuations with the centroid shift w. These results can also be compared with those found for the X-COP sample (Dupourqué et al. 2023), which showed a positive correlation between dynamical indicators that increase with cluster perturbation, specifically the centroid shift w and the Zernike moments. Despite such differences, a Kolmogorov or hydrodynamical cascade (characterized by slopes of −11/3) appears to serve as an appropriate approximation for the turbulence developing in such systems, considering the slopes we obtained are $\alpha = 3.58 \pm 0.11$, including the core, and $\alpha = 3.28 \pm 0.08$, excluding it. The flatter slope in the outer regions might be correlated with a more predominant magnetic field (Vestuto et al. 2003).

The separation of the Tier 1 sample into several mass bins (Figs. 4e and h) shows a non-trivial correlation between mass and variance of the fluctuations. Regarding previous observational constraints, Hofmann et al. (2016) find a mild anti-correlation between relative density fluctuations (or Mach number) and masses, decreasing by a factor of 1.5× from poor to massive clusters. This is in line with our highest and lowest mass bins but not with the intermediate mass bin, which shows much lower normalisations. We note that the low-mass bin does not contain any bin State (I) objects (i.e. the most relaxed clusters in this sample); the high level of normalisation measured can therefore also be linked to the dynamical state within the bin. As for the injection scale, clusters are expected to virialise self-similarly; however, meso- and micro-scale astrophysics introduce key deviations depending on the hydrodynamical process at play (e.g. feedback, condensation, sloshing). For instance, the injection scale tends to reside near the R_{500} region, but lower mass systems are capable of reaching smaller injection scales towards the core region, likely due to the relatively stronger AGN feedback impact (e.g. Gaspari et al. 2014a). The slope is instead roughly invariant with mass, again suggesting a similar type of turbulence (hydrodynamical). The Mass (III) sample is the most comparable to the previous study on X-COP, and it shows comparable variance and slope, but increased injection, which is interpreted as a spatial resolution effect in Sect. 3.2.

The last corner plots (Figs. 4f and i) show the separation of the sample over the Tier 2 redshift range. At high redshifts ($z \gtrsim 1$), galaxy clusters are expected to experience more frequent mergers (e.g. Huško et al. 2022), which can induce stronger turbulence and density fluctuations in the ICM. With increasing redshift, we observe a mild increase in density variance (hence turbulence) and injection scales. However, our redshifts reach, at best, $z \sim 0.5$–0.6, which is far from the early Universe formation. Thus, over the redshift range studied via Tier 2, most turbulence parameters appear to be fairly similar.

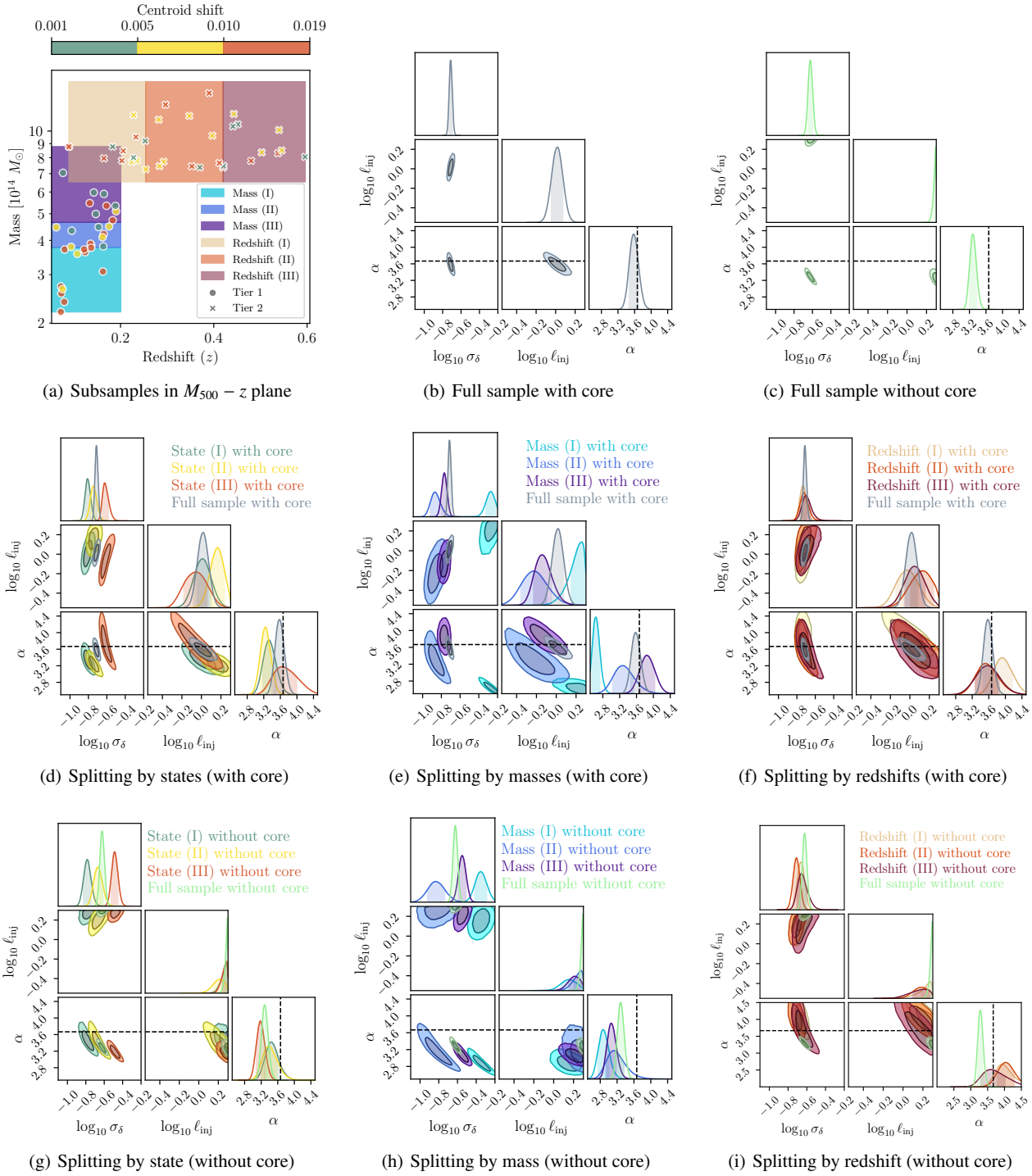

(a) Subsamples in $M_{500} - z$ plane (b) Full sample with core (c) Full sample without core

(d) Splitting by states (with core) (e) Splitting by masses (with core) (f) Splitting by redshifts (with core)

(g) Splitting by state (without core) (h) Splitting by mass (without core) (i) Splitting by redshift (without core)

Fig. 4. Constraints on the density fluctuation parameters in the state, mass, and redshift sub-samples used in this analysis. (a) Distribution of sub-samples in mass-redshift plane. The shaded areas indicate the mass and redshift sub-samples extracted from Tiers 1 and 2, respectively. The colour of the dots reflects the dynamical state of the clusters as measured by the centroid shift w. (b) Joint posterior distributions of the standard deviation, σ_δ, the injection scale, $\ell_{\rm inj}$, and the spectral index α of the density fluctuation power spectrum parameters, evaluated on the full sample including the core $<0.15\,R_{500}$ region and (c) excluding the core region. The dashed black line represents the expected 11/3 index from Kolmogorov theory. (d), (e), and (f) are the same plot using the sub-samples associated with the state, mass, and redshift, respectively, as defined in Table 1, including the core region. (g), (h), and (i) use the same sub-samples without the core regions.

3.2. Effect of core exclusion and spatial resolution

The first differences between the analyses with and without the cluster core involve an increase in fluctuation variance, especially in the Mass (III), State (III), and global results, which might suggest that clusters are more disturbed, on average, in the outer regions. There is also a decrease in the global slope, which could indicate either that the outer regions are noisier due to a lower signal-to-noise ratio or that turbulent processes undergo reinjection at multiple scales, thereby flattening the observed spectrum. Regarding the injection scale, energy injection processes in the cluster cores, such as AGN feedback and sloshing,

have a smaller characteristic scale than the outer regions, which are dominated by accretion and merger events. Our constraints on the injection scale average the low injections in the centre and the high injections from the outer parts. This might explain the reason for which we constrain $\ell_{\rm inj}$ to approximately R_{500} when including the core region but reduce it to an upper limit of roughly $2R_{500}$ – the largest scale that can be measured in our field – when the core is excluded. Using CHEX-MATE, the low angular size of clusters prevents us from properly assessing the low injection scale in the central region; this is due to the low number of pixels in this region. As an illustration, there is a median number of ∼200 pixels below $0.15\,R_{500}$ in CHEX-MATE, compared to ∼10 000 pixels below $0.15\,R_{500}$ in X-COP. However, such behaviour has already been observed in the radial study of X-COP.

Furthermore, as CHEX-MATE clusters are, on average, smaller in the sky than X-COP clusters, the lowest spatial limit that can be exploited on X-COP is 50% smaller than that on CHEX-MATE, which implies a better sampling of the inertial range. This is illustrated in Fig. 1, where the conservative lowest scale we defined is shown along the individual scales that could be achieved for each cluster, and the clusters common to X-COP are on the lower left. This definition for the lowest scale allows consistency of analysis over the whole sample, but results in less sensitivity to small scales found in the core regions of clusters, skewing the results towards larger injection scales. In Fig. 3, the constraints from X-COP align with those from CHEX-MATE when we compare the outer rings, which exclude the core region driving the low injection. Systematically excluding the core from this kind of analysis will reduce the contamination from substructures such as the sloshing spirals, the cool core, or cold fronts from older merger, which further increase the correlation between measured density fluctuations and turbulent process (see Sect. 4.2, for further discussions).

3.3. Correlation with radio data

The presence of turbulence in the ICM is expected to induce particle acceleration through second-order Fermi mechanisms in the turbulent medium (e.g. Brunetti & Lazarian 2016), which could be responsible for the presence of radio haloes in galaxy clusters. Eckert et al. (2017b) showed a bimodality in the distribution of the amplitude of X-SB fluctuations at 150 kpc, separating clusters with and without radio haloes and the correlation between the radio halo power at 1.4 GHz and the 1D Mach number $\mathcal{M}_{\rm 1D}$; this was done using a sample of 51 clusters. More recently, Zhang et al. (2023) performed a similar analysis on a smaller sample of 36 haloes, detected at lower frequencies with LOFAR. Confirmation of the bimodality was not achievable due to the limited sample size. Additionally, no clear indications of a correlation between the velocity dispersion and the radio power at 150 MHz were found, possibly due to the LoTSS DR2 survey containing more objects with an ultra-steep spectrum. These objects experienced less energetic mergers when compared to clusters in Eckert et al. (2017b) (see Brunetti & Jones 2014, for a review). In this section, we use the CHEX-MATE, which is partially covered by the LoTSS (Shimwell et al. 2019), to search for a trend in our density fluctuation model regarding the presence of a radio halo using the whole available spatial scales.

In Fig. 5, we plot the contour obtained for the analysis split into the common clusters with LoTSS DR2, with and without radio halo. We note that, on average, the parameters we examine align well. We do not observe any significant difference between the two sub-samples. It is important to note that the exclusion of the most perturbed clusters leads us to study a population of radio haloes with a homogeneous distribution regarding their dynamical state, as illustrated in Fig. 2. Hence, this population is very different from the populations previously studied in Eckert et al. (2017b) and Zhang et al. (2023), which may justify the absence of a clear trend in our results. The limited sample size hinders the determination of trends between fluctuations and radio haloes in this study, but the upcoming radio coverage of the CHEX-MATE sample (82 clusters in total) will allow for the confirmation or refutation of this trend.

4. Discussions

4.1. Interpretation as turbulent motion

Assuming turbulence in the ICM as the primary source of relative density fluctuations, precursory hydrodynamical and theoretical studies (Gaspari & Churazov 2013; Gaspari et al. 2014b; Zhuravleva et al. 2014a) demonstrated that the characteristic amplitude of turbulent velocity dispersion – which defines the Mach number $\mathcal{M} = \sigma_v/c_{\rm s}$ (with σ_v the 3D velocity dispersion and $c_{\rm s}$ the sound speed) – is linearly tied to the characteristic amplitude of density fluctuations, unlike in non-stratified fluids, where a quadratic trend is expected. This relation has also been studied in the context of turbulence in a box and corroborated for major stratification levels (Mohapatra & Sharma 2019; Shi & Zhang 2019; Mohapatra et al. 2020, 2021). Gaspari & Churazov (2013) initially found the linear scaling relation between the density fluctuations at different scales and the associated Mach number, by testing varying plasma physics (turbulence, thermal conduction, electron-ion equilibration) in high-resolution hydrodynamical simulations of galaxy clusters. As thermal conduction is expected to be highly suppressed in the observed ICM, an argument supported by our nearly Kolmogorov slopes and by theoretical work (e.g. ZuHone & Roediger 2016), the relation from Gaspari & Churazov (2013), involving the peak of the amplitude spectrum, can be simplified to

$$\mathcal{M}_{\rm 3D} \approx 2\sigma_\delta \left(\frac{l_{\rm inj}}{L_{500}}\right)^{-1/5}, \tag{5}$$

where L_{500} is an injection scale of 500 kpc. Accounting for different levels of turbulence and related spectral slopes, this adds a scatter of ∼0.1 dex.

Subsequently, Zhuravleva et al. (2014b) and Gaspari et al. (2014b) retrieved an analogous linear relationship with the 1D Mach number ($\mathcal{M}_{\rm 1D} = \mathcal{M}_{\rm 3D}/\sqrt{3}$):

$$\mathcal{M}_{\rm 1D} \approx (1 \pm 0.3)\,\sigma_\delta. \tag{6}$$

Overall, the above-quoted studies converge toward a linear relation with roughly unitary normalisation with $\mathcal{M}_{\rm 1D}$. Recently, this was also validated in a set of cosmological simulations with a sample of 80 clusters (Zhuravleva et al. 2023), in particular for non-merging systems, which is also the focus of our work. Eq. (5) has a low dependency on the injection scale, and it is comparable to the scaling from Eq. (6). To account for the dispersion between the two relations, we chose to convert the density fluctuations in Mach number using a unity scaling with a dispersion that accounts for the dispersion between Eqs. (5) and (6):

$$\mathcal{M}_{\rm 3D} \approx \sqrt{3} \times (1 \pm 0.4)\,\sigma_\delta. \tag{7}$$

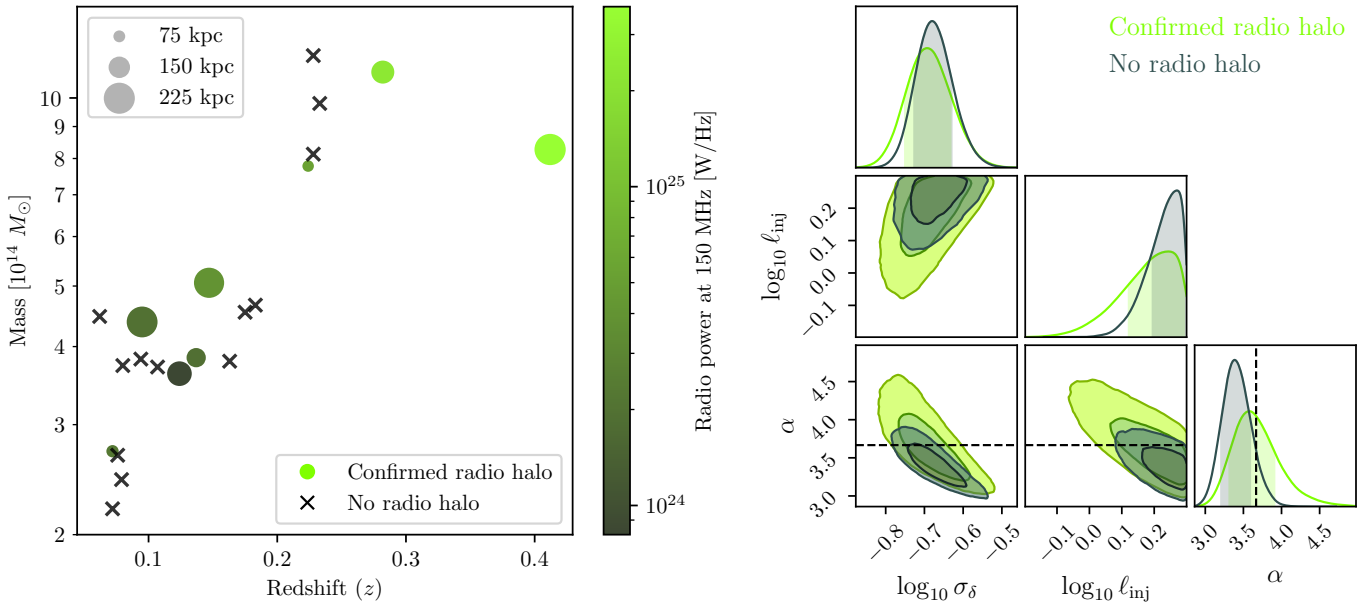

Fig. 5. Density fluctuation analysis with the CHEX-MATE clusters in LoTSS DR2. Left: Visualisation of clusters in LoTSS DR2 in the mass-redshift plane, with estimated halo size and power at 150 MHz. Right: Density fluctuation parameters estimated when using sub-samples with confirmed or excluded radio halo.

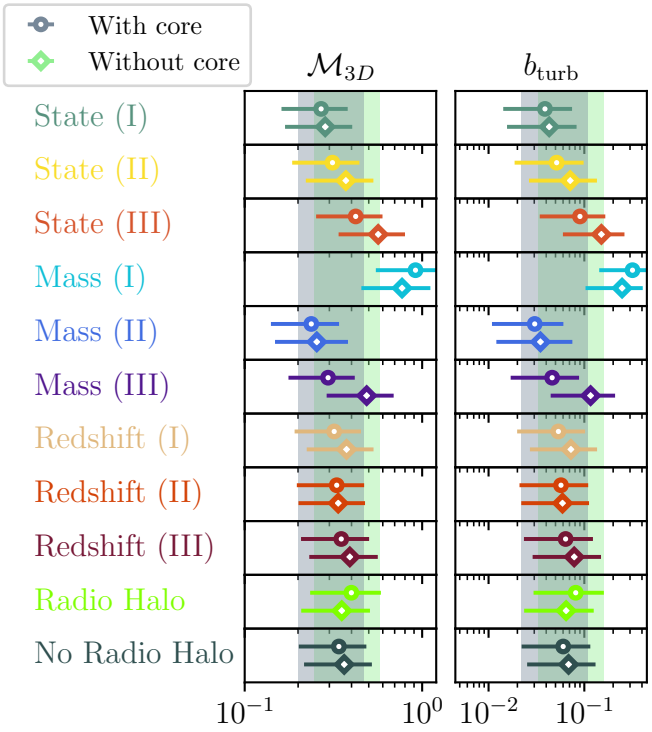

Fig. 6. Mach number $\mathcal{M}_{3D}$ and turbulent mass bias $b_{\rm turb}$ as obtained using relationship from Eqs. (7) and (8), respectively, applied to the dynamical state, the mass, the redshift, and the radio halo sub-samples. The blue and green bands represent the average value over the whole sample with and without the core, respectively. (I) to (III) relate to the increasing value that has been used to define the sub-sample, that is, when increasing disturbance for the state and increasing mass and redshift (see Table 1 for a proper definition of each sub-sample).

Furthermore, we can estimate the contribution of such processes to the non-thermal pressure support globally occurring in our sample. The ratio between the non-thermal pressure and the total pressure can be expressed as a function of the 3D turbulent Mach number $\mathcal{M}_{3D}$ (Eckert et al. 2019) if the non-thermal contribution exclusively comes from turbulence:

$$\frac{P_{\rm turb}}{P_{\rm tot}} = \frac{\mathcal{M}_{3D}^2 \gamma}{\mathcal{M}_{3D}^2 \gamma + 3}, \tag{8}$$

where $\gamma = 5/3$ is the polytropic index. The ratio from Eq. (8) can be directly interpreted as a turbulent mass bias $b_{\rm turb}$ if $\gamma = 5/3$. The Mach numbers and turbulent mass bias $b_{\rm turb}$ deduced in R_{500} are shown in Fig. 6 and Tables B.1 and B.2 for each sub-sample; we used the scaling from Eq. (7), with a $\mathcal{M}_{3D} \simeq 0.41 \pm 0.17$ when evaluated on the whole sample without the core. Consistently with previous studies (e.g. Hofmann et al. 2016) and physical expectations, 3D Mach numbers remain in the subsonic regime, typically in the 0.3–0.5 range. Direct comparison with existing works is not straightforward, as the value of the $\mathcal{M}_{3D}$ derived in this work requires comparison to the 1D velocity broadening measurements. Moreover, the analysis regions we used cover a much larger fraction of the cluster volume than the core region that is probed in most other works. In any case, our results are compatible with subsonic motions as implied by Sanders et al. (2011), Sanders & Fabian (2013) and Pinto et al. (2015). The measured $\mathcal{M}_{3D}$ number value translates into turbulent pressure support of $P_{\rm turb}/P_{\rm tot} \simeq (9 \pm 6)\%$, which is in line with the typical value retrieved in cosmological simulations (e.g. Vazza et al. 2018), and previous observational works on the X-COP sample (Eckert et al. 2019; Dupourqué et al. 2023). The bias of $b = 0.09 \pm 0.06$; the entire considered sample is compatible with the value obtained in Lovisari et al. (2024) when accounting for the fluctuations at all scales, and previous observational works in X-ray (e.g. Eckert et al. 2019; Ettori & Eckert 2022) or using lensing (e.g. Mahdavi et al. 2008; Zhang et al. 2010). As noted in Sect. 3.1, Fig. 6 also shows a clear increase in turbulent Mach numbers towards more disturbed systems, as well as towards lower cluster masses. The redshift trend is instead minor, as expected by our limited range: $z < 0.6$. A complementary approach, proposed by Lovisari et al. (2024), determines the

Mach number and the non-thermal contribution from temperature fluctuations measured on a CHEX-MATE sub-sample. By performing our joint analysis on the same sub-sample, we obtain a Mach number of the order of $\mathcal{M}_{3D} \simeq 0.41 \pm 0.18$, which is compatible with $\mathcal{M}_{3D} \simeq 0.36 \pm 0.10$ as obtained from Lovisari et al. (2024). We note that the resolution of the X-SB maps is better than the resolution of the temperature maps, so the most sensitive scales of turbulence might be different. We stress that these results are derived under the assumption of homogeneous and isotropic turbulence, which, consequently, is described by a Gaussian random field. The stratification of the turbulence, its multi-phase aspect, and its general anisotropies constitute departures from the assumption of Gaussianity. In particular, not taking stratification into account (Mohapatra et al. 2021) and not considering accreted clumps or structural merger remnants may lead to an overestimation of our turbulent Mach number. Accounting for the stochasticity of this process via the sample variance constitutes a non-negligible barrier when it comes to accurately constrain more complex models. Nevertheless, our use of a sample of clusters and the exclusion of central regions limits contamination by clumps, and our use of scaling relations derived from cosmological simulations (Gaspari & Churazov 2013; Simonte et al. 2022; Zhuravleva et al. 2023) partially considers the effect of anisotropies in our final Mach number calculation.

4.2. Discussing the correlation between σ_δ and $\mathcal{M}_{3D}$

The linear link between density fluctuations and turbulent velocities can be analytically derived via simplified hydrodynamics equations for a stratified medium such as the ICM (Gaspari & Churazov 2013; Zhuravleva et al. 2014a). This correlation has been investigated and tested using hydrodynamical simulations (Gaspari & Churazov 2013; Zhuravleva et al. 2014a, 2023; Gaspari et al. 2014b; Simonte et al. 2022). At variance with the above works, Simonte et al. (2022) applied small-scale filtering techniques to disentangle the spurious contribution of bulk flows and extract the isotropic part of turbulent motions, and excised gas clumps in the simulated ICM. Following this approach, they reported a substantially lower normalisation (factor of 2–3) and larger scatter in the above relation, also with significant differences in the slope of the relation, depending on the dynamical state of clusters. They concluded that the presence of residual gas density fluctuations, generally not directly linked to turbulence but to the crossing of self-gravitating clumps and substructures in the ICM, is hard to excise. It introduces a large scatter in the observational link between projected density fluctuations and the true turbulent budget of the ICM. On the other hand, without distinguishing between turbulent and bulk gas motions in the ICM, cosmological runs by Zhuravleva et al. (2023) show such mild/strong correlation and normalisation. To disentangle both sources of fluctuations, a clump-filtering method has to be applied to simulated and observed datasets. Typically, this involves identifying the high-density tail of the gas density distribution. For example, Simonte et al. (2022) cut the top 5% tail, while Zhuravleva et al. (2023) more conservatively cut less than 0.05% of the values (3.5σ). The former reports an applied threshold $\sigma_\delta^2 = 0.22$, hence potentially filtering motions $\mathcal{M}_{1D} \geq 0.47$, which may account for the differences among the various theoretical predictions.

From an observational perspective, it is non-trivial to understand the nature of gas clumping in clusters. Besides filtering obvious mergers, the results of our analysis can be biased toward some residual density structures, which may have varying effects on the parameters depending on their distance from the centre of the cluster, its mass, and its dynamical state. Gas clumps in the outer parts of the cluster will induce high σ_δ as they represent a large relative fluctuation, which could contribute to the correlation between dynamical states and fluctuation normalisations as disturbed clusters contain more substructures. In the central parts, gas clumps are understood as highly significant fluctuations in a very dense region, which will drive the overall spectrum to lower values of σ_δ. The highly structured fluctuations associated with clumps can also bring high slopes and constraints on the injection scale that are close to the clump size. This highlights the challenge of disentangling density fluctuations emerging from turbulent motions and substructures/clumps, such as those also observed in the central parts of X-COP clusters (Dupourqué et al. 2023) and in the CHEX-MATE sample, as illustrated in Fig. C.1. One approach to estimating the contamination due to these substructures could be to use simulations involving contamination by modelled cool-cores or sloshing spirals, and to estimate the biases induced on the reconstruction of the parameters of the fluctuation field as well as the robustness of this approach to the individual deviations of each cluster. This exercise would require the exploration of a large space of contaminant parameters, and it will be the subject of a future study. Nevertheless, the results obtained by excluding the central regions of each cluster should be more robust with regard to the presence of artefacts, as shown by the exclusion of the bullet of PSZ2G266.04−21.25 and other clumps in Fig. C.1.

5. Conclusions

We applied the methodology introduced in Dupourqué et al. (2023) to the CHEX-MATE sample. We focused on a sample of 64 objects, excluding the most disturbed clusters, as our analysis is not suitable for strongly perturbed surface brightness images. We used this sub-sample to characterise the gas density fluctuations through simulation-based inference applied to the power spectrum of surface brightness fluctuations, increasing the statistic by a factor of ∼5 when compared to X-COP. Our main steps were the following.

- We derived the parameters of the density fluctuation spectrum for different CHEX-MATE subsamples. The high sample statistic allows us to define three classes in terms of dynamical state, mass, and redshift. The fluctuations show a normalisation that increases with the dynamical state, which relates to the fact that disturbed clusters tend to have more density fluctuations. We observe an anti-correlation between the mass and normalisation of the fluctuations. The redshift sub-samples show invariant behaviour, which is consistent with the fact that the turbulence within the ICM is not expected to change drastically over the studied redshift range ($z < 0.6$).
- We assessed the effects of cluster core on the overall results by comparing the analysis in R_{500} to the analysis excluding the central $0.15\,R_{500}$ in each cluster. It can be seen that, in particular, the injection scale is no longer constrained when the centre is excluded, which means that the injection we measure is mainly driven by the high signal and low scale processes occurring in the central region, while the signal outside $0.15\,R_{500}$ only allows us to establish lower limits. The core exclusion reduces the contamination from central structures such as the cool cores or sloshing spiral, making a more reliable measurement for the statistics of fluctuations.
- We conducted a correlation analysis between our measurements and radio data from the LoTSS-DR2, investigating

potential relationships between density fluctuation parameters and the presence of radio haloes. No specific trends emerged when comparing individual parameters of clusters with associated radio halo parameters; this is in line with expectations from the population of haloes we studied, which are low-frequency radio haloes in relaxed clusters.
– We interpreted the density fluctuations as resulting from turbulent processes. Using two scaling relations, we derived 3D Mach numbers for various sub-samples defined using the CHEX-MATE sample. We obtained an average $\mathcal{M}_{3D} \simeq 0.4 \pm 0.2$ and a corresponding non-thermal pressure support of $P_{turb}/P_{tot} \simeq 9 \pm 6\%$ or $b_{turb} \simeq 0.09 \pm 0.06$ in R_{500}, which is consistent with what can be found in the literature.

More advanced constraints could be obtained in the future by crossing the fluctuations of the different ICM observables, such as the fluctuations in the SZE, which carry information at further distances from the centre thanks to dependency over n_e instead of n_e^2 for the X-ray emissivity. Pioneering work such as Khatri & Gaspari (2016) and Romero et al. (2023) demonstrated the feasibility of this approach, yet it remains very challenging, even using high-resolution SZ instruments, and integration of the sample variance remains to be completed. In addition, direct and unambiguous measurement of gas motions could be possible in the coming year with XRISM/Resolve (Terada et al. 2021) and in the next decade with the Line Emission Mapper (LEM Kraft et al. 2022) and *Athena*/X-IFU (Barret et al. 2020) through spatially resolved observations of spectral lines' centroid shifts and broadening.

Acknowledgements. E.P., N.C., S.D., and G.W.P. acknowledge the support of CNRS/INSU and CNES. L.L. acknowledges the financial contribution from the INAF grant 1.05.12.04.01. M.D.P. acknowledges support from Sapienza Università di Roma thanks to Progetti di Ricerca Medi 2020, RM120172B32D5BE2 and Medi 2021, RM12117A51D5269B. F.V. acknowledges the financial support from the Cariplo "BREAKTHRU" funds Rif: 2022–2088 CUP J33C22004310003. M.R., I.B., S.E., S.G. acknowledge the financial contribution from the contracts Prin-MUR 2022, supported by Next Generation EU (n.20227RNLY3 the concordance cosmological model: stress-tests with galaxy clusters), ASI-INAF Athena 2019-27-HH.0, "Attività di Studio per la comunità scientifica di Astrofisica delle Alte Energie e Fisica Astroparticellare" (Accordo Attuativo ASI-INAF n. 2017-14-H.0), and from the European Union's Horizon 2020 Programme under the AHEAD2020 project (grant agreement n. 871158). This work was granted access to the HPC resources of CALMIP supercomputing center under the allocation 2022-22052. LOFAR data products were provided by the LOFAR Surveys Key Science project (LSKSP; https://lofar-surveys.org/) and were derived from observations with the International LOFAR Telescope (ILT). LOFAR (van Haarlem 2013) is the Low Frequency Array designed and constructed by ASTRON. It has observing, data processing, and data storage facilities in several countries, that are owned by various parties (each with their own funding sources), and that are collectively operated by the ILT foundation under a joint scientific policy. The efforts of the LSKSP have benefited from funding from the European Research Council, NOVA, NWO, CNRS-INSU, the SURF Co-operative, the UK Science and Technology Funding Council and the Jülich Supercomputing Centre. This research was supported by the International Space Science Institute (ISSI) in Bern, through ISSI International Team project #565 (Multi-Wavelength Studies of the Culmination of Structure Formation in the Universe). This work made use of various open-source packages such as `matplotlib` (Hunter 2007), `astropy` (Astropy Collaboration 2013, 2018), `ChainConsumer` (Hinton 2016), `cmasher` (van der Velden 2020), `sbi` (Tejero-Cantero et al. 2020), `pyro` (Bingham et al. 2019), `jax` (Bradbury et al. 2018), `haiku` (Hennigan et al. 2021), `numpyro` (Bingham et al. 2019; Phan et al. 2019).

References

Anders, E., & Grevesse, N. 1989, Geochim. Cosmochim. Acta, 53, 197
Angelinelli, M., Vazza, F., Giocoli, C., et al. 2020, MNRAS, 495, 864
Arévalo, P., Churazov, E., Zhuravleva, I., Hernández-Monteagudo, C., & Revnivtsev, M. 2012, MNRAS, 426, 1793
Astropy Collaboration (Robitaille, T. P., et al.) 2013, A&A, 558, A33
Astropy Collaboration (Price-Whelan, A. M., et al.) 2018, AJ, 156, 123
Ayromlou, M., Nelson, D., Pillepich, A., et al. 2023, A&A, in press, https://doi.org/10.1051/0004-6361/202348612
Barret, D., Decourchelle, A., Fabian, A., et al. 2020, Astron. Nachr., 341, 224
Bartalucci, I., Molendi, S., Rasia, E., et al. 2023, A&A, 674, A179
Biffi, V., Borgani, S., Murante, G., et al. 2016, ApJ, 827, 112
Bingham, E., Chen, J. P., Jankowiak, M., et al. 2019, J. Mach. Learn. Res., 20, 1
Botteon, A., Shimwell, T. W., Cassano, R., et al. 2022, A&A, 660, A78
Bradbury, J., Frostig, R., Hawkins, P., et al. 2018, JAX: composable transformations of Python+ NumPy programs, https://github.com/google/jax?tab=readme-ov-file#citing-jax
Brüggen, M., & Vazza, F. 2015, in Magnetic Fields in Diffuse Media, eds. A. Lazarian, E. M. de Gouveia Dal Pino, & C. Melioli (Berlin, Heidelberg: Springer Berlin Heidelberg), Astrophys. Space Sci. Lib., 407, 599
Brunetti, G., & Jones, T. W. 2014, IJMPD, 23, 1430007
Brunetti, G., & Lazarian, A. 2016, MNRAS, 458, 2584
Campitiello, M. G., Ettori, S., Lovisari, L. & CHEX-MATE Collaboration 2022, EPJ Web Conf., 257, 00007
Cappellari, M., & Copin, Y. 2003, MNRAS, 342, 345
CHEX-MATE Collaboration (Arnaud, M., et al.) 2021, A&A, 650, A104
Churazov, E., Vikhlinin, A., Zhuravleva, I., et al. 2012, MNRAS, 421, 1123
Clerc, N., Cucchetti, E., Pointecouteau, E., & Peille, P. 2019, A&A, 629, A143
Cucchetti, E., Clerc, N., Pointecouteau, E., Peille, P., & Pajot, F. 2019, A&A, 629, A144
De Luca, F., De Petris, M., Yepes, G., et al. 2021, MNRAS, 504, 5383
Dupourqué, S., Clerc, N., Pointecouteau, E., et al. 2023, A&A, 673, A91
Ebeling, H., Mullis, C. R., & Tully, R. B. 2000, in Mapping the Hidden Universe: The Universe behind the Milky Way – The Universe in HI, eds. R. C. Kraan-Korteweg, P. A. Henning, & H. Andernach (Astronomical Society of the Pacific), ASP Conf. Proc., 218, 79
Eckert, D., Ettori, S., Pointecouteau, E., et al. 2017a, Astron. Nachr., 338, 293
Eckert, D., Gaspari, M., Vazza, F., et al. 2017b, ApJ, 843, L29
Eckert, D., Ghirardini, V., Ettori, S., et al. 2019, A&A, 621, A40
Ettori, S., & Eckert, D. 2022, A&A, 657, L1
Gaspari, M., & Churazov, E. 2013, A&A, 559, A78
Gaspari, M., Brighenti, F., Temi, P., & Ettori, S. 2014a, ApJ, 783, L10
Gaspari, M., Churazov, E., Nagai, D., Lau, E. T., & Zhuravleva, I. 2014b, A&A, 569, A67
Gatuzz, E., Sanders, J. S., Dennerl, K., et al. 2022a, MNRAS, 511, 4511
Gatuzz, E., Sanders, J. S., Canning, R., et al. 2022b, MNRAS, 513, 1932
Gatuzz, E., Sanders, J. S., Dennerl, K., et al. 2023a, MNRAS, 522, 2325
Gatuzz, E., Mohapatra, R., Federrath, C., et al. 2023b, MNRAS, 524, 2945
Ghirardini, V., Eckert, D., Ettori, S., et al. 2019, A&A, 621, A41
Gianfagna, G., Rasia, E., Cui, W., et al. 2023, MNRAS, 518, 4238
Hennigan, T., Cai, T., Norman, T., & Babuschkin, I. 2021, Haiku: Sonnet for JAX, 2020 https://github.com/google-deepmind/dm-haiku?tab=readme-ov-file#citing-haiku
HI4PI Collaboration (Ben Bekhti, N., et al.) 2016, A&A, 594, A116
Hinton, S. 2016, J. Open Source Softw., 1, 45
Hitomi Collaboration (Aharonian, F., et al.) 2016, Nature, 535, 117
Hoffman, M. D., & Gelman, A. 2014, J. Mach. Learn. Res., 15, 1593
Hofmann, F., Sanders, J. S., Nandra, K., Clerc, N., & Gaspari, M. 2016, A&A, 585, A130
Hunter, J. D. 2007, Comput. Sci. Eng., 9, 90
Huško, F., Lacey, C. G., & Baugh, C. M. 2022, MNRAS, 509, 5918
Khatri, R., & Gaspari, M. 2016, MNRAS, 463, 655
Kolmogorov, A. 1941, Dokl. Akad. Nauk SSSR, 30, 301
Kraft, R., Markevitch, M., Kilbourne, C., et al. 2022, arXiv e-prints [arXiv:2211.09827]
Kravtsov, A. V., Vikhlinin, A., & Nagai, D. 2006, ApJ, 650, 128
Lau, E. T., Kravtsov, A. V., & Nagai, D. 2009, ApJ, 705, 1129
Lovisari, L., Forman, W. R., Jones, C., et al. 2017, ApJ, 846, 51
Lovisari, L., Ettori, S., Rasia, E., et al. 2024, A&A, 682, A45
Mahdavi, A., Hoekstra, H., Babul, A., & Henry, J. P. 2008, MNRAS, 384, 1567
McNamara, B. R., & Nulsen, P. E. J. 2012, New J. Phys., 14, 055023
Melin, J.-B., Bartlett, J. G., & Delabrouille, J. 2006, A&A, 459, 341
Mohapatra, R., & Sharma, P. 2019, MNRAS, 484, 4881
Mohapatra, R., Federrath, C., & Sharma, P. 2020, MNRAS, 493, 5838
Mohapatra, R., Federrath, C., & Sharma, P. 2021, MNRAS, 500, 5072
Nelson, K., Rudd, D. H., Shaw, L., & Nagai, D. 2012, ApJ, 751, 121
Nelson, K., Lau, E. T., Nagai, D., Rudd, D. H., & Yu, L. 2014, ApJ, 782, 107
Ogorzalek, A., Zhuravleva, I., Allen, S. W., et al. 2017, MNRAS, 472, 1659
Ota, N., & Yoshida, H. 2016, PASJ, 68, S19
Ota, N., Fukazawa, Y., Fabian, A. C., et al. 2007, PASJ, 59, S351
Papamakarios, G., Pavlakou, T., & Murray, I. 2017, Advances in Neural Information Processing Systems (Curran Associates, Inc.), 30

Papamakarios, G., Sterratt, D., & Murray, I. 2019, Proceedings of the Twenty-Second International Conference on Artificial Intelligence and Statistics (PMLR), 837
Phan, D., Pradhan, N., & Jankowiak, M. 2019, arXiv e-prints [arXiv:1912.11554]
Piffaretti, R., & Valdarnini, R. 2008, A&A, 491, 71
Pinto, C., Sanders, J. S., Werner, N., et al. 2015, A&A, 575, A38
Planck Collaboration XXVII. 2016, A&A, 594, A27
Pratt, G. W., Arnaud, M., Biviano, A., et al. 2019, Space Sci. Rev., 215, 25
Rasia, E., Meneghetti, M., Martino, R., et al. 2012, New J. Phys., 14, 055018
Rasia, E., Meneghetti, M., & Ettori, S. 2013, Astron. Rev., 8, 40
Romero, C. E., Gaspari, M., Schellenberger, G., et al. 2023, ApJ, 951, 41
Roncarelli, M., Gaspari, M., Ettori, S., et al. 2018, A&A, 618, A39
Rossetti, M., Eckert, D., Gastaldello, F., et al. 2024, A&A, 686, A68
Sanders, J. S., & Fabian, A. C. 2013, MNRAS, 429, 2727
Sanders, J. S., Fabian, A. C., & Smith, R. K. 2011, MNRAS, 410, 1797
Schmidt, W., Engels, J. F., Niemeyer, J. C., & Almgren, A. S. 2016, MNRAS, 459, 701
Schuecker, P., Finoguenov, A., Miniati, F., Böhringer, H., & Briel, U. G. 2004, A&A, 426, 387
Shi, X., & Zhang, C. 2019, MNRAS, 487, 1072
Shi, X., Komatsu, E., Nagai, D., & Lau, E. T. 2016, MNRAS, 455, 2936
Shimwell, T. W., Tasse, C., Hardcastle, M. J., et al. 2019, A&A, 622, A1
Shimwell, T. W., Hardcastle, M. J., Tasse, C., et al. 2022, A&A, 659, A1
Simionescu, A., ZuHone, J., Zhuravleva, I., et al. 2019, Space Sci. Rev., 215, 24
Simonte, M., Vazza, F., Brighenti, F., et al. 2022, A&A, 658, A149
Snowden, S. L., Mushotzky, R. F., Kuntz, K. D., & Davis, D. S. 2008, A&A, 478, 615
Sugawara, C., Takizawa, M., & Nakazawa, K. 2009, PASJ, 61, 1293
Tamura, T., Hayashida, K., Ueda, S., & Nagai, M. 2011, PASJ, 63, S1009
Tamura, T., Yamasaki, N. Y., Iizuka, R., et al. 2014, ApJ, 782, 38
Tejero-Cantero, A., Boelts, J., Deistler, M., et al. 2020, J. Open Source Softw., 5, 2505
Terada, Y., Holland, M., Loewenstein, M., et al. 2021, J. Astron. Telesc. Instrum. Syst., 7, 037001
van der Velden, E. 2020, J. Open Source Softw., 5, 2004
van Haarlem, M. P., Wise, M. W., Gunst, A. W., et al. 2013, A&A, 556, A2
Vazza, F., Roediger, E., & Brüggen, M. 2012, A&A, 544, A103
Vazza, F., Angelinelli, M., Jones, T. W., et al. 2018, MNRAS, 481, L120
Vestuto, J. G., Ostriker, E. C., & Stone, J. M. 2003, ApJ, 590, 858
Vikhlinin, A., Kravtsov, A., Forman, W., et al. 2006, ApJ, 640, 691
Voit, G. M., Meece, G., Li, Y., et al. 2017, ApJ, 845, 80
Weisstein, E. W. 1995, Fourier Transform (Wolfram Research, Inc.)
XRISM Science Team 2020, ArXiv e-prints [arXiv:2003.04962]
Zhang, Y.-Y., Okabe, N., Finoguenov, A., et al. 2010, ApJ, 711, 1033
Zhang, X., Simionescu, A., Gastaldello, F., et al. 2023, A&A, 672, A42
Zhang, C., Zhuravleva, I., Markevitch, M., et al. 2024, MNRAS, 530, 4234
Zhuravleva, I., Churazov, E. M., Schekochihin, A. A., et al. 2014a, ApJ, 788, L13
Zhuravleva, I., Churazov, E., Schekochihin, A. A., et al. 2014b, Nature, 515, 85
Zhuravleva, I., Churazov, E., Arévalo, P., et al. 2015, MNRAS, 450, 4184
Zhuravleva, I., Allen, S. W., Mantz, A., & Werner, N. 2018, ApJ, 865, 53
Zhuravleva, I., Chen, M. C., Churazov, E., et al. 2023, MNRAS, 520, 5157
ZuHone, J. A., & Roediger, E. 2016, J. Plasma Phys., 82, 535820301
ZuHone, J. A., Markevitch, M., & Zhuravleva, I. 2016, ApJ, 817, 110
ZuHone, J. A., Miller, E. D., Bulbul, E., & Zhuravleva, I. 2018, ApJ, 853, 180

Appendix A: Fourier transform convention

In this paper, we define the Fourier transform with the classical signal processing convention, namely $(0, -2\pi)$ (see Weisstein (1995)). This pair results in the forward transform highlighted in Eq. A.1 and A.2. We use $\hat{f}$ and $\tilde{f}$ to refer to the 2D and 3D Fourier transforms of a function f, respectively:

$$\mathcal{FT}_{2D}\{f\} \equiv \int \mathrm{d}^2\boldsymbol{\rho}\, f(\boldsymbol{\rho}) e^{-2i\pi \boldsymbol{k}_\rho \cdot \boldsymbol{\rho}} = \hat{f}(\boldsymbol{k}_\rho), \tag{A.1}$$

$$\mathcal{FT}_{3D}\{f\} \equiv \int \mathrm{d}^3\boldsymbol{r}\, f(\boldsymbol{r}) e^{-2i\pi \boldsymbol{k}_r \cdot \boldsymbol{r}} = \tilde{f}(\boldsymbol{k}_r). \tag{A.2}$$

Appendix B: Table with values

The results obtained for the variance of density fluctuations σ_δ, the injection scale ℓ_{inj}, the spectral index α, the 3D Mach number $\mathcal{M}_{3D,}$ and the turbulent mass bias b_{turb} are displayed in Tab. B.1 with the core region included, and in Tab. B.2 they are shown with the 0.15 R_{500} inner region excluded.

Table B.1. Joint marginalised constraints on parameters for each of the sub-samples defined in Tab. 1; uncertainties correspond to the 68% confidence ranges.

Subsample	σ_δ	ℓ_{inj}	α	$\mathcal{M}_{3D}$	b_{turb}
State (I)	0.16 ± 0.01	1.03 ± 0.21	3.34 ± 0.15	0.27 ± 0.11	0.04 ± 0.03
State (II)	0.18 ± 0.02	1.45 ± 0.23	3.24 ± 0.12	0.31 ± 0.13	0.05 ± 0.04
State (III)	0.24 ± 0.02	0.87 ± 0.24	3.71 ± 0.29	0.42 ± 0.17	0.09 ± 0.07
Mass (I)	0.53 ± 0.06	1.62 ± 0.27	2.64 ± 0.09	0.91 ± 0.39	0.32 ± 0.16
Mass (II)	0.14 ± 0.02	0.60 ± 0.20	3.30 ± 0.25	0.24 ± 0.10	0.03 ± 0.03
Mass (III)	0.17 ± 0.01	0.73 ± 0.16	3.85 ± 0.18	0.29 ± 0.12	0.05 ± 0.04
Redshift (I)	0.18 ± 0.02	0.94 ± 0.25	3.94 ± 0.23	0.32 ± 0.13	0.05 ± 0.04
Redshift (II)	0.19 ± 0.02	1.30 ± 0.31	3.56 ± 0.27	0.33 ± 0.14	0.06 ± 0.05
Redshift (III)	0.20 ± 0.03	1.12 ± 0.27	3.57 ± 0.29	0.35 ± 0.15	0.06 ± 0.05
Radio Halo	0.24 ± 0.04	1.48 ± 0.53	3.47 ± 0.47	0.40 ± 0.18	0.08 ± 0.07
No Radio Halo	0.20 ± 0.02	0.84 ± 0.24	3.25 ± 0.19	0.34 ± 0.14	0.06 ± 0.05
Joint	0.19 ± 0.01	1.04 ± 0.14	3.58 ± 0.11	0.34 ± 0.14	0.06 ± 0.04

Table B.2. Joint marginalised constraints on parameters for each of the sub-samples defined in Tab. 1 after exclusion of the central 0.15 R500 region. Uncertainties correspond to the 68% confidence ranges.

Subsample	σ_δ	ℓ_{inj}	α	$\mathcal{M}_{3D}$	b_{turb}
State (I)	0.16 ± 0.02	1.83 ± 0.14	3.46 ± 0.16	0.28 ± 0.12	0.04 ± 0.04
State (II)	0.22 ± 0.02	1.60 ± 0.21	3.41 ± 0.18	0.37 ± 0.16	0.07 ± 0.06
State (III)	0.33 ± 0.03	1.84 ± 0.12	3.19 ± 0.10	0.57 ± 0.23	0.15 ± 0.10
Mass (I)	0.45 ± 0.06	1.42 ± 0.24	2.88 ± 0.13	0.77 ± 0.34	0.25 ± 0.14
Mass (II)	0.15 ± 0.03	1.75 ± 0.19	3.16 ± 0.23	0.25 ± 0.12	0.03 ± 0.04
Mass (III)	0.28 ± 0.03	1.61 ± 0.21	3.07 ± 0.11	0.49 ± 0.20	0.12 ± 0.08
Redshift (I)	0.22 ± 0.02	1.71 ± 0.26	4.00 ± 0.31	0.37 ± 0.16	0.07 ± 0.05
Redshift (II)	0.19 ± 0.02	1.50 ± 0.24	4.05 ± 0.25	0.34 ± 0.14	0.06 ± 0.05
Redshift (III)	0.22 ± 0.03	1.47 ± 0.30	3.70 ± 0.35	0.39 ± 0.17	0.08 ± 0.06
Radio Halo	0.20 ± 0.03	1.55 ± 0.28	3.64 ± 0.31	0.35 ± 0.15	0.06 ± 0.05
No Radio Halo	0.21 ± 0.02	1.72 ± 0.20	3.41 ± 0.19	0.37 ± 0.16	0.07 ± 0.05
Joint	0.24 ± 0.01	1.93 ± 0.07	3.29 ± 0.08	0.41 ± 0.17	0.09 ± 0.06

Appendix C: Fluctuation gallery

The gallery of surface brightness fluctuations on the CHEX-MATE sub-sample used for this analysis is shown in Fig. C.1. These are sorted with increasing values of the centroid shift w.

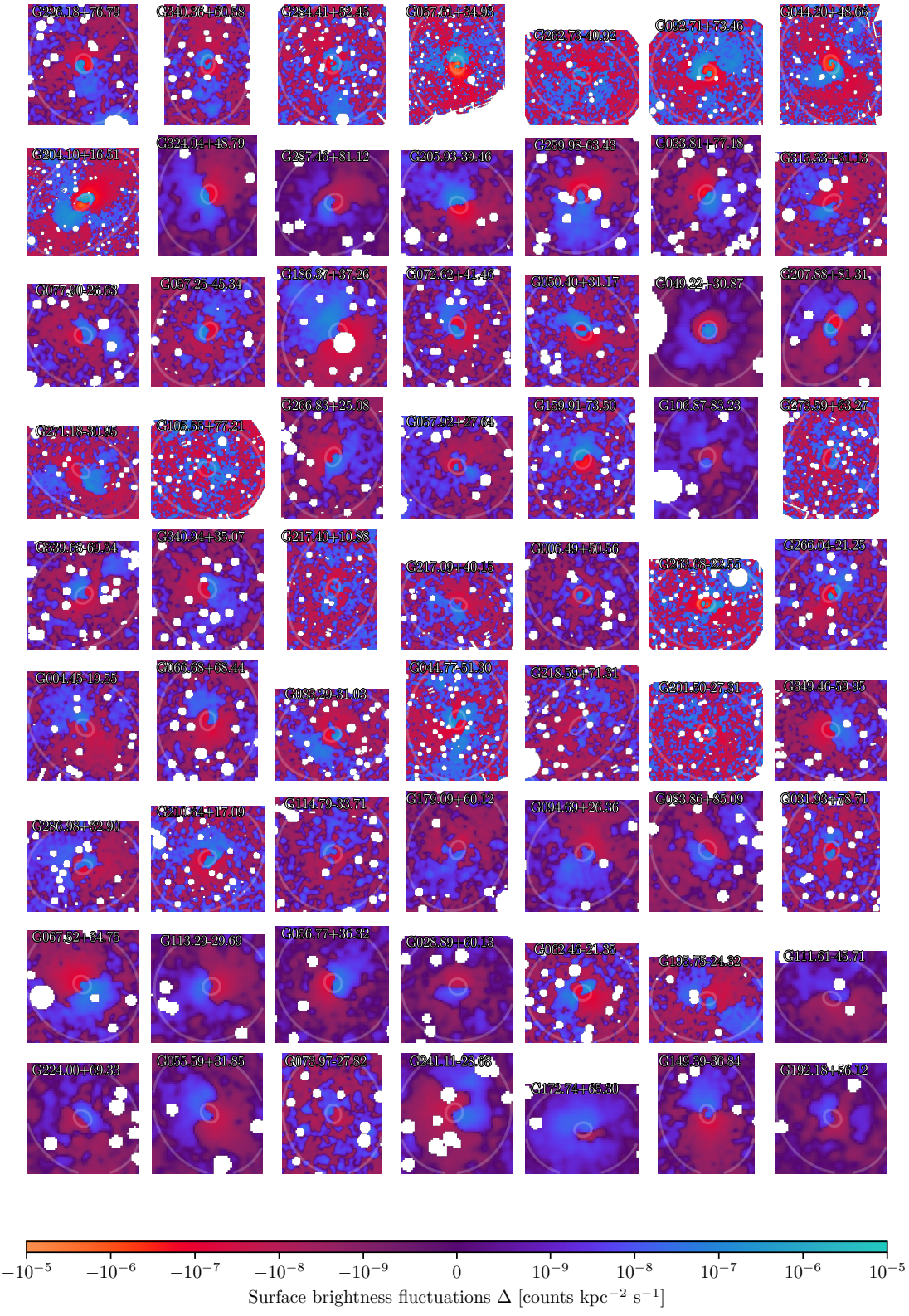

Fig. C.1. Surface brightness fluctuation gallery with masked point sources, as defined in Eq. 2 for the 63 clusters used in the analysis (see Fig. 4a); these are given in ascending order of w. The two rings denote 0.15 and $1R_{500}$.